

# Structured Random Models for Phase Retrieval with Optical Diffusers

Zhiyuan Hu, Fakhriyya Mammadova, Julian Tachella, Michael Unser, Jonathan Dong

**Abstract**—Phase retrieval is a nonlinear inverse problem that arises in a wide range of imaging modalities, from electron microscopy to Fourier ptychography. In particular, the reconstruction is facilitated when the sensing matrix is i.i.d. random, enabling strong theoretical guarantees and efficient reconstruction algorithms. However, its applicability is restricted by excessive computational costs. In this paper, we propose structured random models for phase retrieval, where we emulate a dense random matrix by a cascade of structured transforms and random diagonal matrices. We reduce the complexity from quadratic to log-linear at no cost in reconstruction performance. Through a spectral method initialization followed by gradient descent, robust reconstruction is obtained at an oversampling ratio as low as 2.8. Moreover, we observe that the reconstruction performance is solely determined by the singular-value distribution of the forward matrix. This class of models can directly be implemented with basic optical elements such as lenses and diffusers, paving the way for large-scale phase imaging with robust reconstruction guarantees.

**Index Terms**—Compressed sensing, structured transforms, random matrix theory, nonlinear optimization.

## I. INTRODUCTION

Phase retrieval refers to reconstructing the phase information of a complex-valued field from amplitude-only measurements. It enables the complete characterization of the electric field for label-free imaging and wavefront engineering and pertains to modalities such as astronomy [1], crystallography [2], computer-generated holography [3], [4], optical computing [5], Fourier ptychography [6], electron and optical microscopy [7], [8]. However, the nonlinearity introduced by amplitude-only measurements significantly complicates the reconstruction problem compared to linear models. One key parameter to quantify the reconstruction difficulty is the oversampling ratio (OR), defined as the ratio between the dimension of the measurements and that of the unknown signal. While a high OR facilitates reconstruction, it comes at the cost of additional measurements. Thus, reconstruction under a low OR is desirable.

This work was supported by the Swiss National Science Foundation under Grant PZ00P2\_216211. Julian Tachella acknowledges support by the French ANR grant UNLIP (ANR-23-CE23-0013). (*Corresponding Author: Zhiyuan Hu.*)

Zhiyuan Hu, Fakhriyya Mammadova, Michael Unser and Jonathan Dong are with the Biomedical Imaging Group, École polytechnique fédérale de Lausanne, 1015, Switzerland. (e-mail: zhiyuan.hu@epfl.ch; faxriyya489@kaist.ac.kr; michael.unser@epfl.ch; jonathan.dong@epfl.ch)

Julian Tachella is with LPENSL, CNRS & ENS Lyon, 46 allée de l’Italie, 69364, France. (e-mail: julian.tachella@cnrs.fr)

Existing phase-imaging modalities typically involve Fourier transforms [9]. The earliest occurrence, Fourier phase retrieval [10], reconstructs an image based solely on its Fourier magnitude. This challenging reconstruction problem is made easier when more measurements become available, for instance, through shifts of the source position in ptychography [11], [12] or through several illumination angles in Fourier ptychography [6], [13]. These systems result in a sensing matrix composed of Fourier and diagonal matrices, which enables high-resolution imaging thanks to efficient computation. Despite the observation that more measurements lead to an inverse problem that is easier to solve, theoretical guarantees are lacking to ensure proper reconstructions, even given many measurements. Additionally, algorithms can become trapped in a suboptimal local minimum due to the nonlinear optimization landscape.

Meanwhile, random phase retrieval [14], where the forward operator is an i.i.d. random matrix, benefits from a rich theoretical foundation. Previous studies have established information-theoretic bounds on the reconstruction accuracy as a function of the OR [15], [16], deriving a perfect-recovery threshold at an OR slightly above 2. In practice, efficient dedicated algorithms have also been proposed, for instance, approximate message passing (AMP) [14], [16], [17] and spectral methods [18], [19], [20]. Although corresponding to the physical propagation of waves in a complex medium [14], [21], the random model is rarely implemented in practice due to its prohibitively high computational cost. The  $\mathcal{O}(n^2)$  dense matrix-vector multiplication required to evaluate the forward model makes reconstruction intractable in both space and time for high-resolution imaging.

Interestingly, many recent examples converge toward the replacement of a dense matrix by a fast linear transform. A linear transform of the form  $\mathbf{H}\mathbf{D}$  is employed in compressed sensing [22] and locality-sensitive hashing [23]. It corresponds to a subsampled Hadamard transform associated with a random diagonal matrix, an efficient structured transform that can be evaluated in  $\mathcal{O}(n \log n)$ . In nonlinear models such as neural networks [24], [25], [26] or random features [27], a sequence of efficient transforms (e.g.,  $\mathbf{H}\mathbf{D}\mathbf{H}\mathbf{D}$ ) is used to emulate dense connections. These transforms occur naturally in optics, as they correspond to operations performed by lenses and planar interfaces. Moreover, the multiplication by a random diagonal matrix can be implemented with optical diffusers. They have been introduced in lensless imaging [28], [29], [30]; yet, their applicability to phase imaging has not been investigated.

In this paper, we propose a structured random model to facilitate phase retrieval through a cascade of structured transforms

and random diagonal matrices. We demonstrate that the structured random model enables the same reconstruction quality as dense random models, and is much more computationally efficient. We present that a model architecture composed of two structured transforms and diagonal operations is the minimal setting in which a dense random matrix can be emulated. We also show that the singular-value distribution of the model solely determines the reconstruction performance. In practice, this system can be implemented optically with lenses and diffusers. This framework is highly flexible, as the results remain unchanged with other diffuser phase distributions and structured transforms.

The organization of this paper is as follows: in Section II, we define structured random models for phase retrieval and the corresponding optical systems, and analyze the covariance patterns of the elements in the sensing matrices. In Section III, we provide more details on the reconstruction configuration, including algorithms (gradient descent and spectral methods) and evaluation metrics. In Section IV, we present the evaluation results of the structured random model.

## II. STRUCTURED RANDOM MODEL

In this section, we show that at least 2 structured transforms and random diagonal matrices are needed to obtain a sensing matrix with uncorrelated elements.

### A. Model Definition

The forward model of phase retrieval is

$$\mathbf{y} = |\mathbf{Ax}|^2, \quad (1)$$

with  $\mathbf{x} \in \mathbb{C}^n$  the signal to be reconstructed,  $\mathbf{A} \in \mathbb{C}^{m \times n}$  the sensing matrix, and  $\mathbf{y} \in \mathbb{R}^n$  the measurements. The linear operator  $\mathbf{A}$  depends on the phase-imaging modalities. In the context of dense random models, the elements in  $\mathbf{A}$  are i.i.d. sampled from a complex-valued Gaussian distribution. In ptychography and Fourier ptychography, the forward matrix is a vertical concatenation of  $\mathbf{FD}$  and  $\mathbf{FDF}$ , respectively, where  $\mathbf{F}$  stands for a Fourier matrix and  $\mathbf{D}$  a diagonal matrix. Existing imaging modalities often leverage Fourier transforms and diagonal matrices, as these operations correspond to the ones performed by optical lenses and thin transmissive elements, respectively.

For the structured random model, we define the forward matrix as

$$\mathbf{A} = \mathbf{S} \left( \prod_{i=1}^L \mathbf{FD}_i \right) [\mathbf{F}] \mathbf{O}, \quad (2)$$

where  $\mathbf{D}_i \in \mathbb{C}^{p \times p}$  denotes a diagonal matrix with i.i.d. random diagonal elements of intermediate dimension  $p = \max(m, n)$ . The amplitude and phase of the  $j$ th diagonal element  $d_j^{(i)} = r_j^{(i)} e^{i\theta_j^{(i)}}$  of  $\mathbf{D}_i$  are independently sampled for  $j = 1, \dots, p$ .

The matrix  $\mathbf{F}$  represents the discrete Fourier transform with complex entries

$$\mathbf{F} = [f_{kl}] = \frac{1}{\sqrt{p}} e^{j \frac{2\pi}{p} kl}, \quad (3)$$

where  $k, l$  represent the row and column indices of the entry, respectively.

The undersampling  $\mathbf{S} = [\mathbf{I}_m, \mathbf{0}] \in \mathbb{C}^{m \times p}$  and oversampling  $\mathbf{O} = [\mathbf{I}_n, \mathbf{0}]^T \in \mathbb{C}^{p \times n}$  matrices represent possible trimming and zero-padding operations.

We define  $L$  as the depth (i.e., the number of layers) of the model in Eq. 2, with an optional Fourier transform  $[\mathbf{F}]$  as an additional 0.5 layer. Two important configurations are the **1.5-layer** and **2-layer** structured random transforms, with the respective transform sequence

$$\mathbf{A}_{1.5} = \mathbf{SFD}_1 \mathbf{FO}, \quad (4)$$

$$\mathbf{A}_2 = \mathbf{SFD}_1 \mathbf{FD}_2 \mathbf{O}. \quad (5)$$

For greater generality, the Fourier transform in (2) can be replaced by another structured transform: a dense linear transform that can be evaluated in sub- $\mathcal{O}(n^2)$  complexity. The intuition behind the structured random model stems from the understanding that each of its two key components emulates dense random matrices. In particular, the diagonal matrices introduce randomness while the structured transforms mix the different elements.

The structured random model can be realized practically. We illustrate in Figure 1 the optical systems for both 1.5-layer and 2-layer configurations. Each Fourier transform corresponds to a lens and each diagonal matrix to a diffuser. This hardware setup is simple to build and to calibrate in practice.

We shall use random diagonal matrices  $\mathbf{D}_i$  with:  $\mathbb{E} \left[ \left( r_j^{(i)} \right)^2 \right] = 1$  for asymptotic energy conservation and  $\mathbb{E} \left[ d_j^{(i)} \right] = 0$ .

### B. Covariance Analysis

While the design in (2) permits an arbitrary model depth, the determination of the optimal depth remains crucial from a practical perspective due to the increased complexity inherent with deeper models. This motivates two fundamental questions: (i) whether the structured random model can replicate the statistical properties of a dense random model; and (ii) how many layers are required to obtain such equivalence. To analyze the randomness of the model, we study the covariance between the elements of the sensing matrix  $\mathbf{A}$  as a function of depth. This second-order metric captures the lowest-order dependence between random variables. Moreover, for Gaussian random variables, the multivariate distribution is completely characterized by its first- and second-order moments.

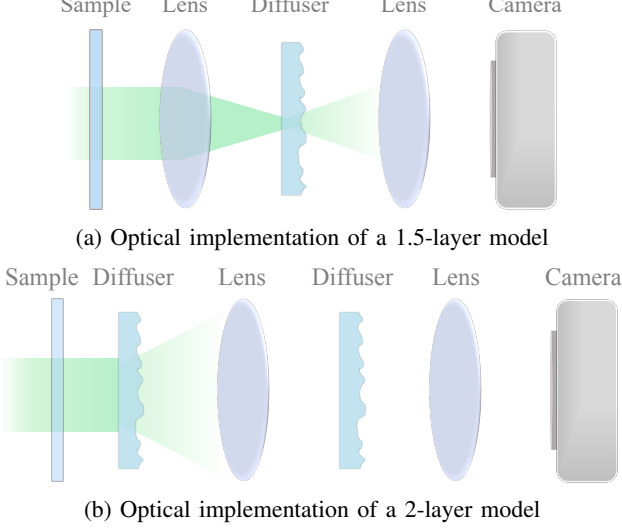


Fig. 1: Optical implementations of structured random models with 1.5 and 2 layers, with each structured transform corresponding to a lens and each random diagonal matrix to a diffuser.

We show in the following that the covariances exhibit distinct patterns. For the computation, we denote the elements in the structured transform and random diagonal matrix as  $\mathbf{F} = [f_{ij}] \in \mathbb{C}^{N \times N}$  and  $\mathbf{D} = \text{diag}([d_i]) \in \mathbb{C}^{N \times N}$ . All results are derived for the case of a square matrix. Since undersampling and oversampling correspond to subsampled versions of this matrix, the extension of the derivation to the general non-square case follows directly.

We now formulate the covariance pattern of a dense i.i.d. matrix and consider the three particular cases that correspond to 1 layer, 1.5 layers, and 2 or more layers.

**Proposition II.1.** *For a dense matrix containing independent elements with variance  $1/N$ , the covariance between two elements at position  $(m, n)$  and  $(k, l)$  is*

$$\text{Cov}(a_{mn}, a_{kl}) = \begin{cases} \frac{1}{N}, & \text{if } m = k \text{ and } n = l \\ 0, & \text{otherwise.} \end{cases} \quad (6)$$

### 1) One Layer:

**Proposition II.2.** *For a 1-layer model, the covariance between two elements in the forward matrix is given by*

$$\text{Cov}(a_{mn}, a_{kl}) = \begin{cases} 0, & \text{if } n \neq l \\ |d_l|^2 f_{mn} \overline{f_{kl}}, & \text{if } n = l. \end{cases} \quad (7)$$

*Proof.* The element at row  $i$  and column  $j$  of the forward matrix of a 1-layer model is:

$$a_{ij} = d_j f_{ij}, \quad (8)$$

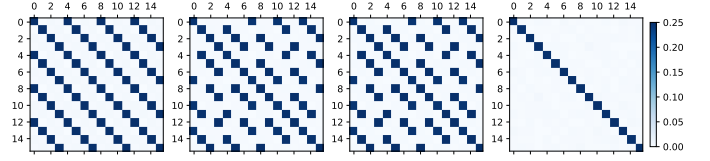


Fig. 2: Covariance matrices of  $(4 \times 4)$  structured random models with different layers using the Fourier transform. Covariance is gradually removed by adding more depth, which produces uncorrelated elements with 2 layers.

The covariance between two elements can be thus computed as

$$\begin{aligned} \text{Cov}(d_n f_{mn}, d_l f_{kl}) &= \mathbb{E} [(d_n f_{mn} - \mathbb{E}[d_n f_{mn}]) (d_l f_{kl} - \mathbb{E}[d_l f_{kl}])] \\ &= \mathbb{E} [d_n f_{mn} \overline{d_l f_{kl}}], \quad (\text{as } \mathbb{E}[d_i] = 0) \end{aligned}$$

which directly yields the result by the independence of the diagonal elements  $d_i$ .  $\square$

Proposition II.2 shows that the resulting matrix exhibits nonzero covariances within each column. This implies that each row of the sensing matrix  $\mathbf{a}_i^H$  is strongly correlated with the others. Since each measurement in  $\mathbf{y}$  is computed as the modulus of the inner product between the signal and one row of  $\mathbf{A}$ , these covariances heavily reduce the effective span of the sensing vectors, thereby making the problem more difficult.

To verify the theoretical derivations, we sample 10000 structured random matrices of size  $4 \times 4$  and compute their empirical covariances between the 16 elements. Figure 2 illustrates the covariance matrices for different model depths. The index  $i$  represents the element position by row  $m = \lfloor i/N \rfloor$ , where  $\lfloor \cdot \rfloor$  is the floor operation, and column  $n = i \bmod N$ . It can be seen that for 1 layer, the elements in the same column have a nonzero covariance.

### 2) One and a Half Layers:

**Proposition II.3.** *For a 1.5-layer model, the forward matrix is left-circulant with asymptotically Gaussian-distributed elements of zero mean and variance  $1/N$ . The covariance pattern is given by*

$$\text{Cov}(a_{mn}, a_{kl}) = \begin{cases} \frac{1}{N}, & \text{if } ((m+n) - (k+l)) \bmod N = 1 \\ 0, & \text{otherwise.} \end{cases} \quad (9)$$

*Proof.* For 1.5 layers, the element at row  $i$  and column  $j$  of the forward matrix is

$$a_{ij} = \sum_{p=1}^N d_p f_{ip} f_{pj}. \quad (10)$$

It is a summation of pseudosamples  $d_p f_{ip} f_{pj}$ , which consist of random samples  $d_p$  and structured modulations  $f_{ip} f_{pj}$ . By the

central limit theorem (CLT), this summation asymptotically follows a Gaussian distribution for large values of  $N$ . The mean of  $a_{ij}$  is zero as each sample  $d_p$  has zero mean. The covariance is computed as

$$\begin{aligned}
& \text{Cov}\left(\sum_{p=1}^N d_p f_{mp} f_{pn}, \sum_{p=1}^N d_p f_{kp} f_{pl}\right) \\
&= \mathbb{E} \left[ \sum_{p=1}^N d_p f_{mp} f_{pn} \sum_{q=1}^N d_q f_{kq} f_{ql} \right] \quad (\mathbb{E}[d_i] = 0) \\
&= \mathbb{E} \left[ \sum_{p=1}^N |d_p|^2 f_{mp} f_{pn} \overline{f_{kp} f_{pl}} \right] \quad (d_i \text{ is i.i.d.}) \\
&= \sum_{p=1}^N f_{mp} f_{pn} \overline{f_{kp} f_{pl}} \quad (\mathbb{E}[|d_p|^2] = 1) \\
&= \sum_{p=1}^N \frac{1}{N^2} e^{j \frac{2\pi}{N} p(k+l-m-n)},
\end{aligned}$$

where the last simplification results from (3). The above covariance pattern shows that the forward matrix is left-circulant, with uncorrelated elements in each row.  $\square$

Figure 2 displays the covariance pattern of a 1.5-layer model, which indeed coincides with the pattern of a left-circulant matrix. Compared to a 1-layer, the covariances in the same column of the sensing matrix are destroyed, but new covariances between different columns are introduced.

### 3) Two or More Layers:

**Proposition II.4.** *For a model of depth  $L \geq 2$  layers, the elements in the forward matrix emulate uncorrelated samples from an asymptotically Gaussian distribution with zero mean and variance  $1/N$ . The covariance is given by*

$$\text{Cov}(a_{mn}, a_{kl}) = \begin{cases} \frac{1}{N}, & \text{if } m = k \text{ and } n = l \\ 0, & \text{otherwise.} \end{cases} \quad (11)$$

*Proof.* We prove Proposition II.4 by induction. For  $L = 2$  layers, the  $i$ th row and  $j$ th column element of the forward matrix is:

$$a_{ij} = d'_j \sum_{p=1}^N d_p f_{ip} f_{pj}. \quad (12)$$

Each element of the forward matrix is then a multiplication of an element of the 1.5-layer model with an extra random sample  $d'_j$ . The element  $a_{ij}$  asymptotically follows a Gaussian distribution according to the CLT, with zero mean since the diagonal elements  $d'_j$  themselves have zero mean. The

covariance is computed as

$$\begin{aligned}
& \text{Cov}\left(d'_n \sum_{p=1}^N d_p f_{mp} f_{pn}, d'_l \sum_{p=0}^N d_p f_{kp} f_{pl}\right) \\
&= \mathbb{E} \left[ d'_n \overline{d'_l} \sum_{p=1}^N |d_p|^2 f_{mp} f_{pn} \overline{f_{kp} f_{pl}} \right] \quad (d_i \text{ is i.i.d.}) \\
&= \mathbb{E} \left[ d'_n \overline{d'_l} \sum_{p=1}^N f_{mp} f_{pn} \overline{f_{kp} f_{pl}} \right] \quad (\mathbb{E}[|d_p|^2] = 1) \\
&= \mathbb{E} \left[ d'_n \overline{d'_l} \sum_{p=1}^N \frac{1}{N^2} e^{j \frac{2\pi}{N} p(k+l-m-n)} \right] \quad (\text{Equation (3)}) \\
&= \begin{cases} \frac{1}{N}, & \text{if } ((m+n) - (k+l)) \bmod N = 0 \text{ and } n = l \\ 0, & \text{otherwise,} \end{cases}
\end{aligned}$$

which gives (11) as  $((m+n) - (k+l)) \bmod N = 0$  implies that  $m+n = k+l$ .

We then assume that Proposition II.4 holds true for  $L \geq 2$ . For depth  $L+0.5$ , the corresponding model is  $\mathbf{A}_{L+0.5} = \mathbf{A}_L \mathbf{F}$ . As  $a_{ij}^{(L+0.5)} = \sum_{p=1}^N a_{ip}^{(L)} f_{pj}$ , each element also follows an asymptotic Gaussian distribution with zero mean in reason of the CLT. The covariance can be computed as

$$\begin{aligned}
& \text{Cov}\left(\sum_{p=1}^N a_{mp}^{(L)} f_{pn}, \sum_{p=1}^N a_{kp}^{(L)} f_{pl}\right) \\
&= \mathbb{E} \left[ \sum_{p=1}^N a_{mp}^{(L)} f_{pn} \sum_{q=1}^N a_{kq}^{(L)} f_{ql} \right] \quad (\mathbb{E}[a_{ij}^{(L)}] = 0) \\
&= \begin{cases} \sum_{p=1}^N \mathbb{E}[|a_{mp}^{(L)}|^2] f_{pn} \overline{f_{pl}}, & \text{if } m = k \\ 0, & \text{otherwise} \end{cases} \\
& \quad (a_{ij}^{(L)} \text{ uncorrelated}) \\
&= \begin{cases} \frac{1}{N}, & \text{if } m = k \text{ and } n = l \\ 0, & \text{otherwise.} \end{cases}
\end{aligned}$$

The last equality follows from the fact that  $a_{ij}^{(L)}$  has zero mean and variance  $1/N$ , and that the Fourier matrix  $\mathbf{F}$  is unitary.

For depth  $L+1$ , the model is  $\mathbf{A}_{L+1} = \mathbf{A}_{L+0.5} \mathbf{D}$ , each element  $a_{ij}^{(L+1)} = a_{ij}^{(L+0.5)} d_j$  also following an asymptotic Gaussian distribution with zero mean. The covariance can be computed as

$$\begin{aligned}
& \text{Cov}(a_{mn}^{(L+0.5)} d_n, a_{kl}^{(L+0.5)} d_l) \\
&= \mathbb{E} \left[ a_{mn}^{(L+0.5)} \overline{a_{kl}^{(L+0.5)}} d_n \overline{d_l} \right] \quad (\mathbb{E}[a_{ij}^{(L+0.5)}] = 0) \\
&= \begin{cases} \frac{1}{N}, & \text{if } m = k \text{ and } n = l, \\ 0, & \text{otherwise.} \end{cases}
\end{aligned}$$

$\square$

The extra sample  $d'_j$  in 2 layers further decouples the elements in different columns, destroying the remaining covariances in a 1.5-layer model. As verified in Figure 2, the covariance matrix of a 2-layer model is diagonal.

### III. METHODS

In this section, we describe the algorithms used to obtain the reconstruction from the measurements. We focus on gradient descent and spectral methods as they offer a good balance between performance and efficiency. Furthermore, we describe the experimental setup for the evaluations, including the signal and model configurations as well as algorithm and evaluation metric choices.

#### A. Gradient Descent

Gradient descent (GD) is a general-purpose iterative method for nonlinear optimization. The gradient of the loss function can often be derived in closed form. For instance, the gradient of the standard  $\ell_2$  loss

$$\mathcal{L}(\hat{\mathbf{x}}) = \|\mathbf{A}\hat{\mathbf{x}}\|^2 - \mathbf{y}\|^2, \quad (13)$$

is given by

$$\nabla_{\hat{\mathbf{x}}}\mathcal{L} = -2\mathbf{A}^H \text{diag}(\hat{\mathbf{x}})(\mathbf{y} - \mathbf{A}\hat{\mathbf{x}})^2, \quad (14)$$

where  $\text{diag}(\cdot)$  denotes the diagonal matrix whose diagonal is the argument vector. The evaluation of the gradient involves matrix multiplications with both the forward matrix  $\mathbf{A}$  and its adjoint  $\mathbf{A}^H$ . In general, the complexity is determined by the structure of the forward model, while some momentum techniques, such as the Nesterov acceleration [31], utilize the historical information collected throughout the iterates to further accelerate the convergence.

Despite an abundance of available algorithms, GD lacks convergence guarantees for phase retrieval due to the theoretical difficulty introduced by the nonlinearity. To improve convergence in practice, we typically use spectral methods as an initialization of GD to improve its convergence.

#### B. Spectral Methods

Spectral methods (SM) make for a class of reconstruction algorithms specific to the quadratic nature of phase retrieval. They aim to find the leading eigenvector of the covariance matrix [19], [20], [32]

$$\mathbf{M}_{\mathcal{T}} = \frac{1}{m} \sum_{i=1}^m \mathcal{T}(y_i) \mathbf{a}_i \mathbf{a}_i^H = \mathbf{A}^H \text{diag} \left( \frac{\mathcal{T}(\mathbf{y})}{m} \right) \mathbf{A}, \quad (15)$$

where  $y_i$  is the  $i$ th element of the measurements  $\mathbf{y}$ ,  $\mathbf{a}_i^H$  the  $i$ th row of the sensing matrix  $\mathbf{A}$ , and  $\mathcal{T}$  an increasing preprocessing function used to assign weights to the outer products  $\mathbf{a}_i \mathbf{a}_i^H$ . The intuition is that each measurement  $y_i$  represents the magnitude of the inner product between  $\mathbf{x}$  and  $\mathbf{a}_i$ , and reflects their covariance. A larger  $y_i$  suggests that  $\mathbf{a}_i$  is more closely aligned with  $\mathbf{x}$  and should be assigned a heavier weight. Among all preprocessing functions, the optimal one for Gaussian i.i.d. random phase retrieval has been derived as  $\mathcal{T}(y) = \max(1 - 1/y, -b)$ , where  $b > 0$  defines a lower bound

for negative eigenvalues [20]. The covariance matrix  $\mathbf{M}_{\mathcal{T}}$  is a second-order quantity that should provide a bias towards  $\mathbf{x}$  in its principal eigenvector. Although SM can be applied to any forward-matrix configuration, theoretical and numerical studies have largely focused on the i.i.d. random case.

In practice, the principal eigenvector is obtained through power iterations. Starting from a random initial guess  $\hat{\mathbf{x}}_0$ , we iteratively compute

$$\hat{\mathbf{x}}_{t+1} = \mathbf{M}_{\mathcal{T}} \hat{\mathbf{x}}_t + 2b\hat{\mathbf{x}}_t, \quad (16)$$

where  $t$  is the iteration index. The trailing term  $2b\hat{\mathbf{x}}_t$  serves as regularization against negative eigenvalues. While GD can be trapped in local minima, SM is guaranteed to converge to the original signal.

#### C. Experimental Setup

1) *Model Setup:* We evaluate the performance of the 2-layer structured random model  $\mathbf{A} = \mathbf{SFD}_1 \mathbf{FD}_2 \mathbf{O}$ , with  $\mathbf{F}$  applied by the fast Fourier transform (FFT). The choice of the number of layers will be further investigated in Section IV-C. The phase of the diagonal elements of  $\mathbf{D}_1$  and  $\mathbf{D}_2$  are sampled uniformly between 0 and  $2\pi$  and the diagonal elements of  $\mathbf{D}_1$  all have unit magnitude. To emulate i.i.d. random matrices, we sample the squared amplitudes of the diagonal elements of  $\mathbf{D}_2$  from the Marchenko-Pastur distribution, which describes the asymptotic eigenvalue distribution of  $\mathbf{X}^H \mathbf{X}$ , where  $\mathbf{X} \in \mathbb{C}^{m \times n}$  is an i.i.d. sampled Gaussian matrix. With  $\lambda_{\pm} = \sigma^2(1 \pm \sqrt{1/\alpha})^2$ , where  $\sigma^2$  is the variance of the sampling Gaussian distribution of  $\mathbf{X}$ . This distribution is given by

$$\mathcal{MP}_{\alpha}(\lambda) = \max(0, 1 - \alpha)\delta(\lambda) + \mathbf{1}_{[\lambda_-, \lambda_+])(\lambda)}\nu(\lambda), \quad (17)$$

in which  $\delta$  is a Dirac distribution and  $\mathbf{1}_{[\lambda_-, \lambda_+]}$  is the indicator function of  $[\lambda_-, \lambda_+]$ . The bulk distribution is

$$\nu(\lambda) = \frac{\alpha\sqrt{(\lambda_+ - \lambda)(\lambda - \lambda_-)}}{2\pi\sigma^2\lambda}. \quad (18)$$

2) *Signal Configuration:* We use the standard Shepp-Logan image of  $(64 \times 64)$  pixels as the phase information of the signal to be reconstructed. The grayscale pixel values are mapped linearly from  $[0, 1]$  to a phase in  $[-\pi, \pi]$ . The magnitudes of the phase signal are set to be constant and equal to 1. In later sections, we consistently use the Shepp-Logan image as the phase image, unless otherwise specified, while we keep the image size.

3) *Algorithms Configuration:* We use GD and SM, either separately or together, with SM returning an initial guess for the GD iterations. We fix the hyperparameters as follows: for SM, the preprocessing function is  $\mathcal{T}(y) = \max(1 - 1/y, -b)$  with regularization parameter  $b = 10$ ; the mean of  $\mathbf{y}$  is renormalized to be 1; we also set a maximum of 5,000 power iterations with early stopping upon convergence. For GD, the maximal number of iterations is 10,000 with early stopping, and the stepsize is chosen as  $2/L$ , where  $L$  is an

estimated upper bound of the local Lipschitz constant of the loss function computed at the initial guess. We let the numbers of iterations to ensure the convergence of each algorithm. Although the amplitude loss  $\mathcal{L}(\hat{\mathbf{x}}) = \|\mathbf{A}\hat{\mathbf{x}}\| - \|\mathbf{y}\|^2$  is known to provide a more robust performance than the vanilla  $\ell_2$  loss in practice [6], it provides the same performance for the noiseless setting in our case.

4) *Evaluation Metric*: Since the phase-retrieval problem is invariant to a global phase factor, in the sense that, both  $\mathbf{x}$  and  $\mathbf{x}e^{j\phi}$  will generate identical measurements, we use the cosine similarity metric to benchmark reconstruction accuracy. It is given by

$$\cos(\mathbf{x}_{\text{gt}}, \hat{\mathbf{x}}) = \frac{|\mathbf{x}_{\text{gt}}^H \hat{\mathbf{x}}|}{\|\mathbf{x}_{\text{gt}}\| \cdot \|\hat{\mathbf{x}}\|}, \quad (19)$$

where  $\mathbf{x}_{\text{gt}}$  is the ground-truth signal and  $\hat{\mathbf{x}}$  the reconstructed signal. This metric computes the alignment between two signals as a scalar in the range  $[0, 1]$ , where 0 indicates no alignment and 1 represents a perfect reconstruction.

5) *Estimation of Signal Norms*: As the principal eigenvector returned by SM always has unit norm, we only acquire the direction of the signal. However, the quality of the initial guess of the norm is important for the subsequent GD iterations. We estimate the  $\ell_2$ -norm of  $\mathbf{x}$  using the statistics of  $\mathbf{y}$  and  $\mathbf{A}$  as

$$\|\mathbf{x}\|_2 \approx \sqrt{\frac{\mu_y}{\sigma_A^2}}, \quad (20)$$

where  $\mu_y$  and  $\sigma_A^2$  are the sample mean of  $\mathbf{y}$  and sample element-wise variance of  $\mathbf{A}$ , respectively.

A detailed derivation is as follows. The  $i$ th entry of  $\mathbf{y}$  can be written as

$$y_i = \mathbf{x}^H \mathbf{a}_i \mathbf{a}_i^H \mathbf{x}. \quad (21)$$

Given that the rows  $\mathbf{a}_i^H$  are independent, the measurements  $y$  can be treated as independent random variables. Taking the expectation of  $y_i$  yields that

$$\begin{aligned} \mathbb{E}[y_i] &= \mathbb{E}[\mathbf{x}^H \mathbf{a}_i \mathbf{a}_i^H \mathbf{x}] \\ &= \text{Var}[\mathbf{a}_i^H \mathbf{x}] + |\mathbb{E}[\mathbf{a}_i^H \mathbf{x}]|^2 \quad (\text{variance property}) \\ &= \text{Var}[\mathbf{a}_i^H \mathbf{x}] \quad (a_{ij} \text{ with zero mean}) \\ &= \text{Var}[\mathbf{A}] \|\mathbf{x}\|_2^2. \end{aligned}$$

6) *Code Availability*: The proposed forward models and the corresponding reconstruction algorithms are implemented using DeepInverse [33], an open-source computational imaging library. Our complete source code is made publicly available<sup>1</sup>.

## IV. RESULTS

In this section, we demonstrate the reconstruction equivalence between dense and structured random models, followed by a computational benchmark that validates the efficiency of

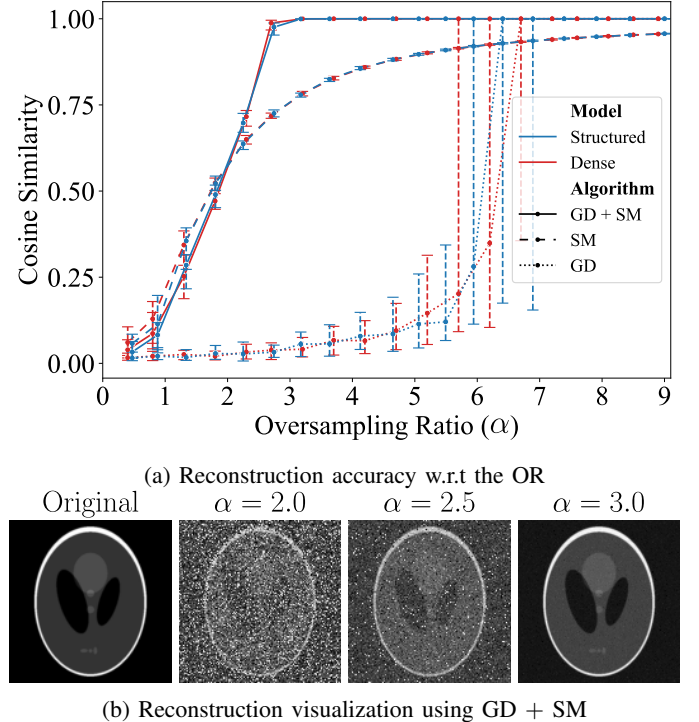


Fig. 3: Reconstruction Comparison. Structured random models obtain the same accuracy as dense random models for each benchmarked algorithm, achieving a perfect recovery at an OR of 2.8.

the structured random model. For a better understanding of the model structure, a comparison on different model depths shows that at least 2 layers are indeed necessary to reproduce the results obtained with i.i.d. random models. We further demonstrate the practicality of the proposed model by showing its robustness to measurement noise, and its flexibility by introducing binary phase diffusers and other structured transforms. Finally, we show that the performance of the model relies on the spectrum of the sensing matrix.

### A. Reconstruction Performance

We first evaluate the reconstruction performance with both dense and structured random models. Figure 3 illustrates (a) the reconstruction performance w.r.t. the OR and provides (b) a few reconstructed images at several key ORs for structured random models. The error bars represent the 10%, 50%, and 90% percentiles among 50 runs, respectively. We show in Figure 3a that structured random models enable a robust reconstruction as good as in the case of dense random models using the same algorithms, which offers an applicable alternative without any performance compromise.

Regarding the choice of algorithms, standalone SM provides a stable and satisfactory performance, while a subsequent run of GD further improves the results. The perfect recovery retrieved at an OR of 2.8 is comparable to the 2.03 threshold

<sup>1</sup><https://github.com/zhiyuhuicode/structured-random-phase-retrieval-v2>

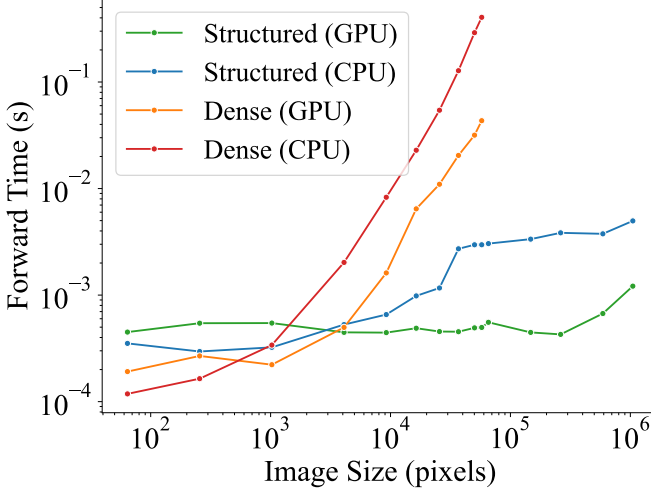


Fig. 4: Time benchmark of the forward pass of dense and structured random models under an OR of 1. Structured random models reach nearly constant forward time on the GPU for moderate image sizes, whereas dense random models quickly become prohibitively slow.

by AMP, and below the typical ORs of 4 in classic phase-imaging modalities. Moreover, standalone GD with random initialization performs significantly worse than GD with SM initialization, thus, unfavorable in practice. This arises from the highly nonconvex loss landscape induced by the phase-retrieval problem, which causes GD to become trapped in local minima. SM mitigates this difficulty by providing a suitable initialization in the attraction basin of the solution.

As illustrated in Fig. 3b, a reconstruction under the OR of 2.0 outlines the general structure of the original object. One can capture more fine-grained details by increasing the OR to 2.5 and, eventually, enabling a perfect recovery at an OR of 3.0.

### B. Computation Benchmark

To demonstrate the speed advantage of structured random models, we benchmark the forward time (i.e., the time to evaluate  $\mathbf{y} = |\mathbf{Ax}|^2$ ) for dense and structured random models w.r.t. the size of the input. The forward pass is evaluated during each iteration of the reconstruction algorithms and is the determining factor for the computational complexity.

We report in Figure 4 the average over 100 runs of the forward time of both models for an OR of 1 on CPU Intel Xeon Gold 6240 and GPU NVIDIA Tesla V100 SXM2. Due to GPU parallelization, the structured random model reaches a nearly constant forward time for moderate image sizes (fewer than  $10^6$  pixels, which corresponds to a  $(1,024 \times 1,024)$  image). In comparison, the forward time of a dense random model resembles a quadratic curve, which matches the theoretical prediction and becomes excessively large already for small image sizes with  $10^4$  pixels. For CPU, the forward time of the structured model remains manageable for small image

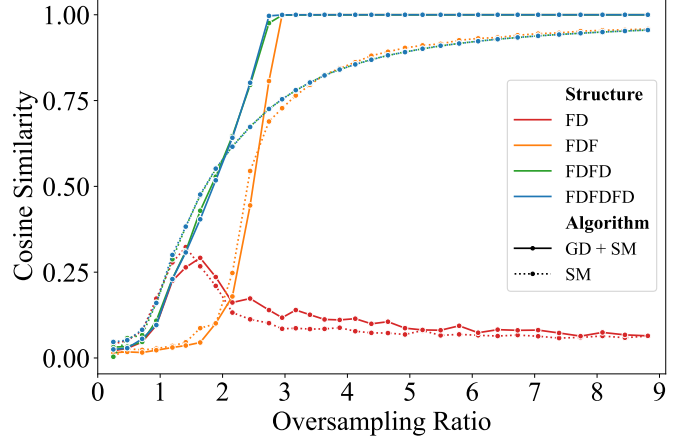


Fig. 5: Performance of structured random models with different depths. A 1-layer model is unable to reconstruct, regardless of its OR, while a 1.5-layer model yields suboptimal performance. A model with more than 2 layers produces the same performance as a dense random model.

sizes with fewer than  $10^5$  pixels, whereas the dense random models are prohibitively slow. For sizes smaller than  $10^3$  pixels, overheads make the structured models a few times slower than the dense ones, although both computational costs are negligible at these modest sizes.

Our benchmark for dense random models is limited to image sizes smaller than  $10^5$  pixels, in reason of the excessive memory requirements of dense matrices. Those scale quartically w.r.t. the number of pixels per edge. For instance, a dense random matrix would consume 17.18 GB for a  $(256 \times 256)$  image. At the same image size, the storage needed for the proposed structured random model is around 1 MB, as only the diagonal matrices need to be stored. This is an improvement of a factor 17,000.

### C. Depth

As the complexity of the imaging system grows with the model depth, we investigate how the reconstruction performance is affected by the number of structured layers. Figure 5 illustrates the performance of the model with different depths. For all models, the amplitude of the rightmost diagonal elements is sampled according to the Marchenko-Pastur distribution, while all the other diagonal elements have a unit amplitude. We conclude from the results that a 1-layer model fails to produce informative measurements for meaningful recovery, regardless of the OR. Meanwhile, the 1.5-layer model enables reasonable reconstructions, although its performance consistently falls short compared to the 2-layer case across all ORs. Furthermore, all models with 2 or more layers yield a performance equivalent to the i.i.d. Gaussian case, as seen in Figure 3a. These observations suggest that an optical system with 2 layers is sufficient to emulate i.i.d. random models in practice.

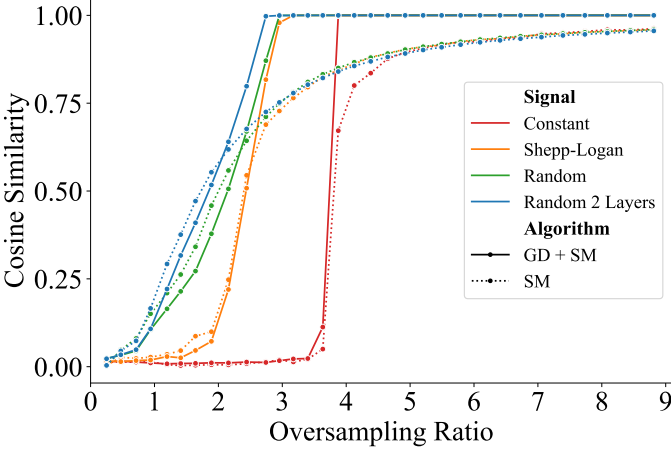


Fig. 6: Performance comparison between different signals with the 1.5-layer structured random model. The performance improves when the input signal has a larger phase variance. The performance approaches that of a 2-layer model when the input signal is random.

#### D. Input-Dependent Reconstruction of One and a Half Layers

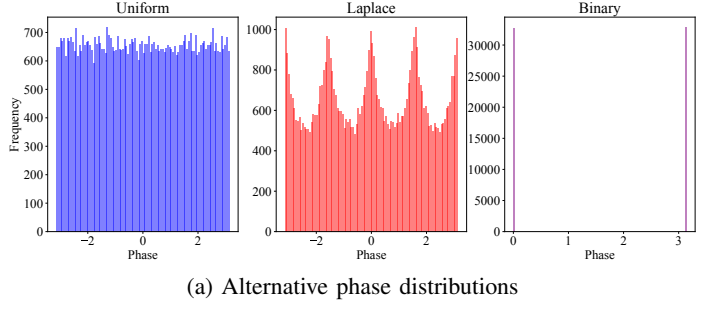
As shown in Section II-B2, the covariance pattern of the sensing matrix resembles a left-circulant matrix. The reconstruction in this case depends on the input signal to recover. We report in Figure 6 the reconstruction performance of several signals in the 1.5 layer case. Beside the Shepp-Logan signal, we use a constant signal where all phases are zero, and a random signal whose phases are uniformly distributed in  $[-\pi, \pi]$ . We conclude from Figure 6 that a better performance can be obtained if one increases the variance of the phase distribution of the signal. Specifically, the performance for a random signal with 1.5 layers is close to that with 2 layers. We explain this behavior by expressing the signal in the Fourier domain as  $\mathbf{x} = \mathbf{F}^H \tilde{\mathbf{x}} \mathbf{F}$ , such that the measurements become  $\mathbf{y} = |\mathbf{F} \mathbf{D}_1 \tilde{\mathbf{x}} \mathbf{F}|^2$ . Ideally, one would like  $\mathbf{D}_1 \tilde{\mathbf{x}}$  to retain all the random elements of  $\mathbf{D}_1$ . However, for a constant signal—or, more generally, for weak-phase objects—the Fourier transform  $\tilde{\mathbf{x}}$  is sparse and the measurements  $\mathbf{y}$  depend on very few diagonal elements of  $\mathbf{D}_1$ .

#### E. Binary Phase Distribution

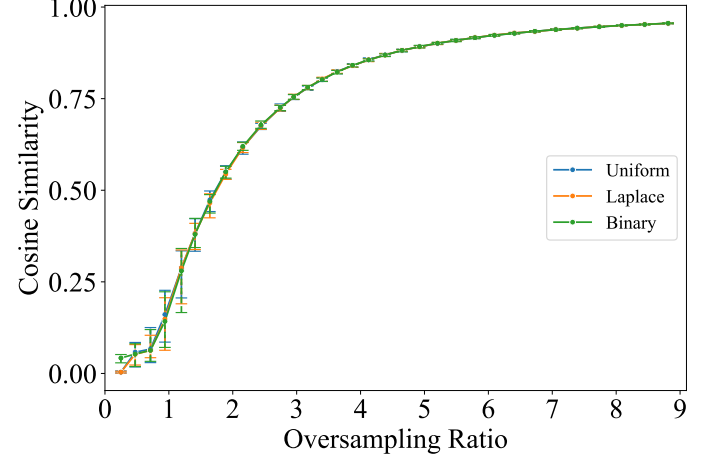
To explore the generality of our structured random model, we experiment with three phase distributions for the phase  $\theta_j$  in the diagonal elements  $d_j = r_j e^{i\theta_j}$ :

- 1) Uniform: uniform distribution on  $[-\pi, \pi]$ ;
- 2) Laplace: distribution of  $\arctan 2(y, x)$ , where  $x$  and  $y$  are drawn from a standard Laplace distribution;
- 3) Binary: uniform distribution in  $\{0, \pi\}$ .

We provide in Figure 7a a histogram of a realization of a phase that follows these three distributions and observe that they are substantially different. Despite this, we see in Figure 7b



(a) Alternative phase distributions



(b) Performance of the alternative phase distributions

Fig. 7: Performance comparison for different phase distributions, including the uniform, Laplace, and binary distributions. Fig. (a) depicts the distributional difference between the alternatives. Fig. (b) shows that the reconstruction performance remains identical despite the distributional difference.

that all options produce the same result. In particular, the binary distribution can greatly simplify the manufacture of the diffusers as it corresponds to only 2 discrete values. Additionally, the diagonal matrices at different layers can share identical elements, which would allow all diffusers to be manufactured from the same template.

The observed universality can be understood if one considers that the diagonal elements are effectively summed through the Fourier transform. Due to the central limit theorem, this summation leads the resulting matrix elements to approach a complex-valued Gaussian distribution, independently of the specific distribution of the diagonal entries.

#### F. Robustness to Noise

To examine the robustness of the structured random model, we apply additive white Gaussian noise to the clean measurement and set

$$\mathbf{y} = \max(|\mathbf{A}\mathbf{x}|^2 + \epsilon, 0), \quad (22)$$

where  $\epsilon \sim \mathcal{N}(\mathbf{0}, \sigma_\epsilon^2 \mathbf{I})$  with  $\sigma_\epsilon = \eta \mu_{|\mathbf{A}\mathbf{x}|^2}$  and  $\eta \in [0, 1]$  controls the strength of the noise relative to the average of the clean measurements  $\mu_{|\mathbf{A}\mathbf{x}|^2}$ . Fig. 8 displays the reconstruction

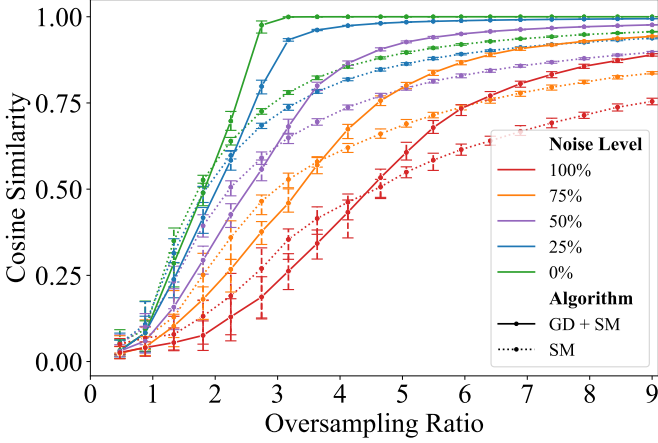


Fig. 8: Performance of the 2-layer structured random model under different noise levels. A good reconstruction is maintained at an OR of 4 under a noise level of 50% of the average of the clean measurements.

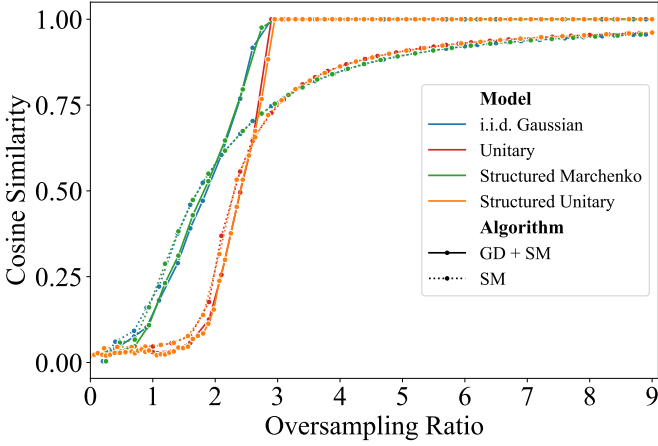


Fig. 9: Performance comparison between the structured and dense random models under different singular spectra. Structured models can yield the same performance as dense models with the same spectrum.

performance of a 2-layer structured random model under different noise levels. The model exhibits strong robustness to noise, maintaining a steady reconstruction even with a noise of 50% of the average of the clean measurements. At higher noise levels, the performance at typical ORs (3–4) is considerably reduced but can be improved by increasing the OR to 6–7.

### G. Spectrum

We observe that the spectrum is the determining factor that characterizes the performance of structured and dense random models. For the 2-layer forward matrix  $\mathbf{A} = \mathbf{F}_1 \mathbf{D}_1 \mathbf{F}_2 \mathbf{D}_2 \mathbf{O}$  with  $\text{OR} > 1$  and  $\mathbf{D}_1$  a unit-magnitude configuration, the

spectrum can be extracted through the Gramian

$$\begin{aligned} \mathbf{A}^H \mathbf{A} &= \mathbf{O}^H \mathbf{D}_2^H \mathbf{F}_2^H \mathbf{D}_1^H \mathbf{F}_1^H \mathbf{F}_1 \mathbf{D}_1 \mathbf{F}_2 \mathbf{D}_2 \mathbf{O} \\ &= \text{diag}(\mathbf{r}_2^2)_{1:n}, \quad (\mathbf{F}_1, \mathbf{D}_1, \mathbf{F}_2 \text{ are all unitary}) \end{aligned}$$

where  $\mathbf{r}_2$  represents the magnitude of the diagonal elements of  $\mathbf{D}_2$  and  $\text{diag}(\cdot)_{1:n}$  denotes the  $(n \times n)$  part of a diagonal matrix on the top-left corner. This shows that the eigenvalues of the Gramian are the first  $n$  elements of  $\mathbf{r}_2^2$ , which are equal to the squared spectrum of the 2-layer model. Therefore, a 2-layer model can easily emulate dense Gaussian or unitary matrices, with the Marchenko-Pastur distribution or units for  $\mathbf{a}_2$ , respectively. We compare in Figure 9 the performance of the structured random models with Marchenko-Pastur distribution for  $\mathbf{D}_2$  or all unitary diagonals with their dense counterparts. We observe that the structured setups match the performance of the dense models. This also explains the low dependence of the performance on the phase distribution, since the latter does not alter the spectrum.

In the undersampled case, the spectrum is obtained from  $\mathbf{A} \mathbf{A}^H$ , which retains the same nonzero support as the sampling distribution of  $\mathbf{r}_2$  beside the expected  $(n - m)$  vanishing singular values, as guaranteed by the Cauchy interlacing theorem [34]. This distributional shift has little effect on overall performance.

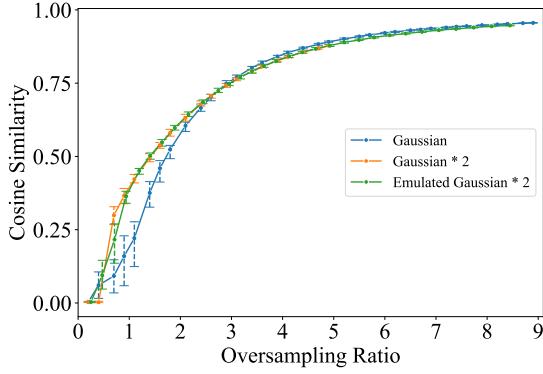
The direct configuration also generalizes to the spectrum of any matrix, for instance, products of i.i.d. Gaussian matrices. A product of  $N$  random Gaussian matrices,  $\mathbf{A} \in \mathbb{C}^{m \times n}$ , is defined as

$$\mathbf{A} = \prod_{i=1}^N \mathbf{X}_i, \quad (23)$$

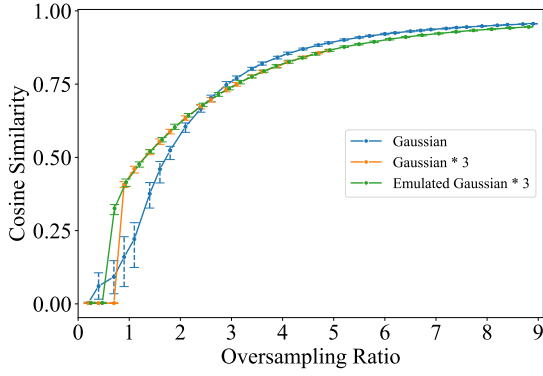
where  $\mathbf{X}_N \in \mathbb{C}^{m \times n}$  and  $\mathbf{X}_i \in \mathbb{C}^{m \times m}, \forall i \in [1, \dots, N-1]$  are i.i.d. sampled from a complex Gaussian distribution  $\mathcal{CN}(0, 1/m)$ . We compare in Figure 10 the performance of the dense random model using a product of 2 to 4 Gaussian matrices to that of their structured random counterparts using the spectra from the dense models. We conclude that the structured random model can lead to the same results as the dense random model when oversampling. Notably, the results are better than that of i.i.d. models at low ORs. When  $\text{OR} < 1$ , the performance differs as undersampling alters the spectrum. This generalizes the use of structured random model to any dense random matrix, as they need no more than the sole knowledge of the spectrum.

### H. Alternative Transforms

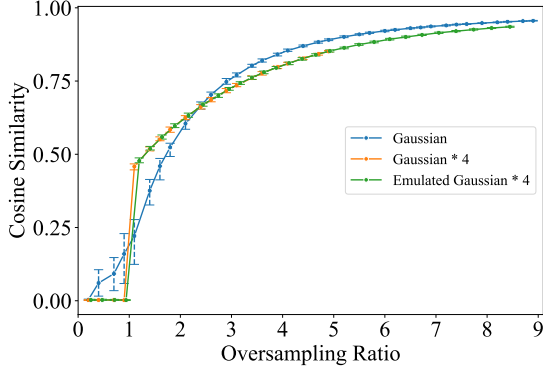
In addition to the FFT, in this section, we investigate two more unitary structured transforms: the discrete cosine transform (DCT) and the Hadamard transform (HT). Like the FFT, these transforms can also be evaluated in  $\mathcal{O}(n \log n)$  time, and can be treated as real-valued proxies for the FFT. We show in Figure 11a the results of the FFT and DCT. Both transforms yield identical results. For the HT, additional padding is needed as the HT only admits the input dimension



(a) 2 Gaussians



(b) 3 Gaussians



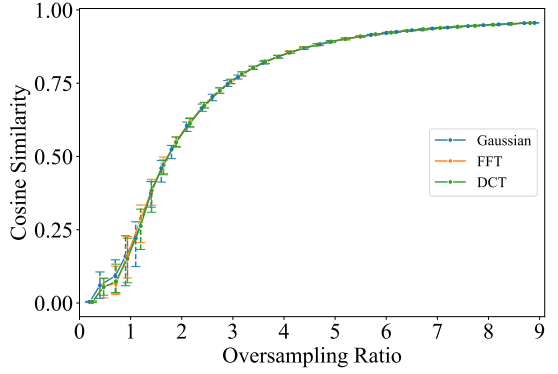
(c) 4 Gaussians

Fig. 10: Performance of products of Gaussian models. Structured models can emulate dense models by using the same spectrum.

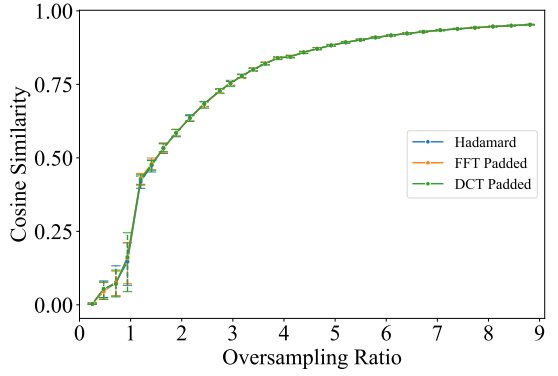
to be  $p = 2^k$ ,  $k \in \mathbb{N}$ . To control this factor, we apply the same over- and undersampling for the FFT, DCT, and HT, which leads to the performance that we report in Figure 11b. All employed transforms generate identical results.

## V. CONCLUSION

We have proposed to replace dense random models, traditionally and in phase retrieval, by a structured random model. This allows us to obtain the same reconstruction accuracy as dense models at a fraction of their original computational costs. Our model is straightforward to realize with practical lenses



(a) Alternative transforms;



(b) Alternative transforms with additional padding;

Fig. 11: Performance comparison of the models using FFT, DCT and HT. All transforms yield the same performance.

and diffusers. The diffusers need only a random binary phase pattern and can share the same realization. Strong robustness to the measurement noise has also been demonstrated. For an optimal architecture, we have shown that two layers are the necessary and sufficient setup for the optimal performance. They are required to generate uncorrelated and asymptotically Gaussian-distributed elements for the overall forward matrix. Further, we have shown that the spectrum of the forward matrix determines the performance of the model. By configuring the spectrum through certain diagonal matrices, we can emulate any dense model. As a result, alternative phase distributions and structured transforms can be used to obtain the same performance, as they maintain the same spectrum. Our work contributes to the growing body of applications that leverage efficient transforms [23], [25], [27], and holds a significant potential for computational accelerations across diverse domains. Finally, our proposed model provides a natural testbed for the exploration of more sophisticated reconstruction algorithms [35], including accelerated first-order methods with classic regularization [36], [37] and learned regularization approaches [38], [39].

## REFERENCES

[1] J. R. Fienup and C. Dainty, “Phase retrieval and image reconstruction for astronomy,” *Image Recovery: Theory and Application*, vol. 231, p. 275, 1987.

[2] D. Sayre, "Some implications of a theorem due to Shannon," *Acta Crystallographica*, vol. 5, no. 6, pp. 843–843, 1952.

[3] J. Zhang, N. Pégard, J. Zhong, H. Adesnik, and L. Waller, "3D computer-generated holography by non-convex optimization," *Optica*, vol. 4, no. 10, pp. 1306–1313, 2017.

[4] M. H. Eypbosh, N. W. Caira, M. Atisa, P. Chakravarthula, and N. C. Pégard, "DeepCGH: 3D computer-generated holography using deep learning," *Optics Express*, vol. 28, no. 18, pp. 26 636–26 650, 2020.

[5] S. Gupta, R. Gribonval, L. Daudet, and I. Dokmanić, "Don't take it lightly: Phasing optical random projections with unknown operators," *Advances in Neural Information Processing Systems*, vol. 32, 2019.

[6] L.-H. Yeh, J. Dong, J. Zhong, L. Tian, M. Chen, G. Tang, M. Soltanolkotabi, and L. Waller, "Experimental robustness of Fourier ptychography phase retrieval algorithms," *Optics Express*, vol. 23, no. 26, pp. 33 214–33 240, 2015.

[7] G. Zheng, R. Horstmeyer, and C. Yang, "Wide-field, high-resolution Fourier ptychographic microscopy," *Nature Photonics*, vol. 7, no. 9, pp. 739–745, 2013.

[8] A. Boniface, J. Dong, and S. Gigan, "Non-invasive focusing and imaging in scattering media with a fluorescence-based transmission matrix," *Nature Communications*, vol. 11, no. 1, p. 6154, 2020.

[9] J. Dong, L. Valzania, A. Maillard, T.-a. Pham, S. Gigan, and M. Unser, "Phase retrieval: From computational imaging to machine learning: A tutorial," *IEEE Signal Processing Magazine*, vol. 40, no. 1, pp. 45–57, 2023.

[10] J. R. Fienup, "Phase retrieval algorithms: a comparison," *Applied Optics*, vol. 21, no. 15, pp. 2758–2769, 1982.

[11] R. G. Paxman, T. J. Schulz, and J. R. Fienup, "Joint estimation of object and aberrations by using phase diversity," *JOSA A*, vol. 9, no. 7, pp. 1072–1085, 1992.

[12] J. Rodenburg and A. Maiden, "Ptychography," *Springer Handbook of Microscopy*, pp. 819–904, 2019.

[13] L. Bian, J. Suo, G. Zheng, K. Guo, F. Chen, and Q. Dai, "Fourier ptychographic reconstruction using wirtinger flow optimization," *Optics express*, vol. 23, no. 4, pp. 4856–4866, 2015.

[14] C. A. Metzler, M. K. Sharma, S. Nagesh, R. G. Baraniuk, O. Cossairt, and A. Veeraraghavan, "Coherent inverse scattering via transmission matrices: Efficient phase retrieval algorithms and a public dataset," in *2017 IEEE International Conference on Computational Photography (ICCP)*. IEEE, 2017, pp. 1–16.

[15] M. Mondelli and A. Montanari, "Fundamental limits of weak recovery with applications to phase retrieval," *Foundations of Computational Mathematics*, vol. 19, no. 3, 2019.

[16] A. Maillard, B. Loureiro, F. Krzakala, and L. Zdeborová, "Phase retrieval in high dimensions: Statistical and computational phase transitions," *Advances in Neural Information Processing Systems*, vol. 33, 2020.

[17] P. Schniter, S. Rangan, and A. K. Fletcher, "Vector approximate message passing for the generalized linear model," in *2016 50th Asilomar Conference on Signals, Systems and Computers*. IEEE, 2016, pp. 1525–1529.

[18] M. Guizar-Sicairos and J. R. Fienup, "Phase retrieval with transverse translation diversity: a nonlinear optimization approach," *Optics Express*, vol. 16, no. 10, pp. 7264–7278, 2008.

[19] J. Ma, R. Dudeja, J. Xu, A. Maleki, and X. Wang, "Spectral method for phase retrieval: an expectation propagation perspective," *IEEE Transactions on Information Theory*, vol. 67, no. 2, pp. 1332–1355, 2021.

[20] W. Luo, W. Alghamdi, and Y. M. Lu, "Optimal spectral initialization for signal recovery with applications to phase retrieval," *IEEE Transactions on Signal Processing*, vol. 67, no. 9, pp. 2347–2356, 2019.

[21] S. M. Popoff, G. Lerosey, R. Carminati, M. Fink, A. C. Boccara, and S. Gigan, "Measuring the transmission matrix in optics: An approach to the study and control of light propagation in disordered media," *Phys. Rev. Lett.*, vol. 104, p. 100601, Mar 2010. [Online]. Available: <https://link.aps.org/doi/10.1103/PhysRevLett.104.100601>

[22] S. Oymak, B. Recht, and M. Soltanolkotabi, "Isometric sketching of any set via the restricted isometry property," *Information and Inference: A Journal of the IMA*, vol. 7, no. 4, pp. 707–726, 2018.

[23] N. Ailon and B. Chazelle, "The fast johnson–lindenstrauss transform and approximate nearest neighbors," *SIAM Journal on computing*, vol. 39, no. 1, pp. 302–322, 2009.

[24] M. Moczulski, M. Denil, J. Appleyard, and N. de Freitas, "ACDC: A structured efficient linear layer," in *4th International Conference on Learning Representations, ICLR 2016, San Juan, Puerto Rico, May 2-4, 2016, Conference Track Proceedings*, Y. Bengio and Y. LeCun, Eds., 2016. [Online]. Available: <http://arxiv.org/abs/1511.05946>

[25] J. Dong, R. Ohana, M. Rafayelyan, and F. Krzakala, "Reservoir computing meets recurrent kernels and structured transforms," *Advances in Neural Information Processing Systems*, vol. 33, pp. 16 785–16 796, 2020.

[26] G. A. D'Inverno and J. Dong, "Comparison of reservoir computing topologies using the recurrent kernel approach," *Neurocomputing*, vol. 611, p. 128679, 2025.

[27] F. X. X. Yu, A. T. Suresh, K. M. Choromanski, D. N. Holtmann-Rice, and S. Kumar, "Orthogonal random features," *Advances in neural information processing systems*, vol. 29, 2016.

[28] N. Antipa, G. Kuo, R. Heckel, B. Mildenhall, E. Bostan, R. Ng, and L. Waller, "Diffusercam: lensless single-exposure 3d imaging," *Optica*, vol. 5, no. 1, pp. 1–9, 2017.

[29] V. Boominathan, J. K. Adams, J. T. Robinson, and A. Veeraraghavan, "Phlatcam: Designed phase-mask based thin lensless camera," *IEEE transactions on pattern analysis and machine intelligence*, vol. 42, no. 7, pp. 1618–1629, 2020.

[30] E. Bezzam, Y. Perron, and M. Vetterli, "Towards robust and generalizable lensless imaging with modular learned reconstruction," *IEEE Transactions on Computational Imaging*, vol. 11, pp. 213–227, 2025.

[31] Y. Nesterov, "A method for solving the convex programming problem with convergence rate  $o(1/k^2)$ ," *Dokl akad nauk Sssr*, vol. 269, p. 543, 1983.

[32] A. Maillard, F. Krzakala, Y. M. Lu, and L. Zdeborová, "Construction of optimal spectral methods in phase retrieval," in *Mathematical and Scientific Machine Learning*, vol. 145. PMLR, 2021, pp. 1–28.

[33] J. Tachella, M. Terris, S. Hurault, A. Wang, D. Chen, M.-H. Nguyen, M. Song, T. Davies, L. Davy, J. Dong, P. Escande, J. Hertzich, Z. Hu, T. I. Liaudat, N. Laurent, B. Levac, M. Massias, T. Moreau, T. Modrzyk, B. Monroy, S. Neumayer, J. Scanvic, F. Sarron, V. Sechaud, G. Schramm, R. Vo, and P. Weiss, "Deepinverse: A python package for solving imaging inverse problems with deep learning," 2025. [Online]. Available: <https://arxiv.org/abs/2505.20160>

[34] J. R. Magnus and H. Neudecker, *Matrix differential calculus with applications in statistics and econometrics*. John Wiley & Sons, 2019.

[35] S. Ducotterd, Z. Hu, M. Unser, and J. Dong, "Undersampled phase retrieval with image priors," *arXiv preprint arXiv:2509.15026*, 2025.

[36] A. Beck and M. Teboulle, "A fast iterative shrinkage-thresholding algorithm for linear inverse problems," *SIAM journal on imaging sciences*, vol. 2, no. 1, pp. 183–202, 2009.

[37] A. Chambolle and T. Pock, "An introduction to continuous optimization for imaging," *Acta Numerica*, vol. 25, pp. 161–319, 2016.

[38] K. H. Jin, M. T. McCann, E. Froustey, and M. Unser, "Deep convolutional neural network for inverse problems in imaging," *IEEE transactions on image processing*, vol. 26, no. 9, pp. 4509–4522, 2017.

[39] S. K. Devalla, P. K. Renukanand, B. K. Sreedhar, G. Subramanian, L. Zhang, S. Perera, J.-M. Mari, K. S. Chin, T. A. Tun, N. G. Strouthidis *et al.*, "Drunet: a dilated-residual u-net deep learning network to segment optic nerve head tissues in optical coherence tomography images," *Biomedical optics express*, vol. 9, no. 7, pp. 3244–3265, 2018.